

RECENT DEVELOPMENT IN QUANTUM MECHANICS/MOLECULAR MECHANICS MODELING FOR MATERIALS

*Xu Zhang, Yi Zhao, & Gang Lu**

Department of Physics and Astronomy, California State University Northridge, Northridge, CA

*Address all correspondence to Gang Lu, E-mail: ganglu@csun.edu

We have introduced two quantum mechanics/molecular mechanics approaches for materials modeling. One is based on quantum mechanical coupling and the other on mechanical coupling. The formalism of both approaches is described in detail. The validations of the methods are demonstrated in terms of atomic and electronic structure. Finally, the applications of the methods are surveyed, including applications in vacancy clusters, dislocations, nanoindentations, and fractures.

KEY WORDS: *quantum coupling, mechanical coupling, defects*

1. INTRODUCTION

Despite the ever-increasing computational power, modeling and simulation of complex material systems at the atomic level still remain a challenge (Lu and Kaxiras, 2004). For example, quantum mechanics (QM) is necessary for a proper treatment of bond-breaking, charge transfer, electron excitation, magnetism, etc., in materials; however, owing to its computational demand, the application of QM has been limited to relatively small systems consisting of up to a few hundreds of atoms. On the other hand, atomistic simulations based on empirical interatomic potentials are often capable of describing small-amplitude vibrations and torsions, elastic deformation, electrostatic interactions, etc., in many materials systems. Termed as molecular mechanical (MM) methods, these empirical atomistic approaches can treat millions of atoms or more. The quantum mechanics and molecular mechanics (QM/MM) coupling algorithms by combining the accuracy of QM descriptions with the low computational cost of MM modeling can thus offer a promising solution to the computational challenge in materials science (Lu and Kaxiras, 2004; Lin and Truhlar, 2007; Bernstein et al., 2009; Mordasini and Thiel, 1998; Woo et al., 1999; Sherwood, 2000; Gao and Truhlar, 2002; Zhang and Lu, 2007).

In a QM/MM simulation, the computational domain is partitioned into two regions: Region I is the primary region where QM simulations are performed and region II is the surrounding region where classical atomistic simulations are carried out. The coupling between regions I and II is at the heart of any QM/MM method. Various schemes have been developed to treat the interaction between the QM and MM regions. Depending on the formulation of the interaction energy, the QM/MM methods can be divided into two categories: mechanical coupling and quantum coupling. In mechanical coupling, one performs quantum mechanical simulation of region I in the absence of region II, and treats the interactions between the regions I and II at the MM level. On the other hand, in the quantum coupling, the quantum mechanical calculation for region I is carried out in the presence of region II; a single-particle embedding potential that represents the quantum mechanical effects of region II enters the QM Hamiltonian of region I.

The advantage of the mechanical coupling is simplicity (Liu et al., 2007). It demands nothing beyond what is required for a density functional theory (DFT) cluster calculation and two classical MM calculations (one for bulk and the other for a cluster). On the other hand, the quantum coupling allows a more accurate description, in particular, for the electronic structure of region I. For example, the fictitious surface states due to the cluster calculation of region I

in the mechanical coupling can be eliminated in the quantum coupling (Zhang et al., 2008). Of course, the quantum coupling is, in general, more complicated than the mechanical coupling.

For many molecular systems that are of interest in chemistry and biochemistry, one can partition the system by cutting the chemical bonds linking the QM and MM parts and then saturate the dangling bonds at the boundary of QM region by so-called link atoms (Lin and Truhlar, 2007; Gao and Truhlar, 2002). This procedure and similar ones can be justified because of the presence of well-defined and localized chemical bonds in such molecular systems. Indeed, the mechanical coupling that is based on the cutting/saturating chemical bonds has seen wide applications in chemistry and biochemistry (Lin and Truhlar, 2007; Gao and Truhlar, 2002). On the other hand, for metallic materials, the procedure is no longer valid owing to the delocalized nature of metallic bonding; it becomes impractical to cut and saturate bonds. In fact, the very concept of the bond becomes less appropriate than the band picture for metals. Therefore, more sophisticated ideas have to be developed to deal with metallic cohesion represented by the delocalized electron states across the QM/MM boundary. The present paper focuses on the recent development of such ideas for modeling metallic materials.

In Section 2, we present the methodology for both quantum coupling and mechanical coupling. The validations of the both methods are described in Section 3. We present applications of the two coupling approaches in Section 4, followed by a summary in Section 5.

2. METHODOLOGY

Although different levels of QM simulations could be employed in region I, we focus on the Kohn-Sham density functional theory (KS-DFT) (Kohn and Sham, 1965). Similarly, although many empirical potentials could be used in region II, we choose the embedded-atom method (EAM) (Daw and Baskes, 1984) as an example of MM calculations in the paper. The total energy of a system, including the energy of the region I, the energy for the region II, and the interaction energy between them, can be expressed as

$$E_{\text{tot}}[\text{I} + \text{II}] = E_{\text{KS}}[\text{I}] + E^{\text{int}}[\text{I}, \text{II}] + E_{\text{MM}}[\text{II}] \quad (1)$$

In the quantum coupling, the interaction energy $E^{\text{int}}[\text{I}, \text{II}]$ is formulated by DFT; on the other hand, $E^{\text{int}}[\text{I}, \text{II}]$ is calculated by EAM in the mechanical coupling approach.

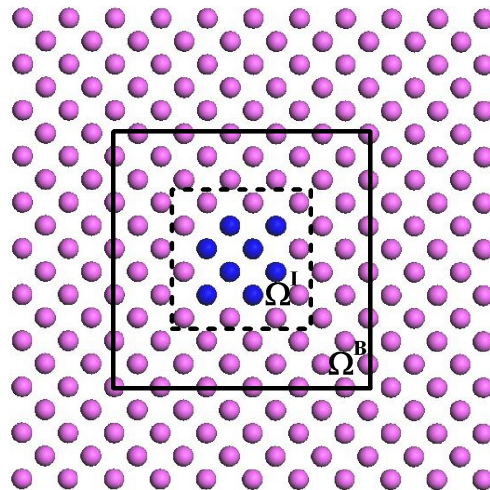


FIG. 1: Schematic diagram of the partitioned system. Blue and magenta spheres represent the atoms belonging to region I and region II, respectively. The dashed box represents Ω^{I} , and the solid box represents the periodic box Ω^{B} .

2.1 Quantum Coupling

The self-consistent determination of the interaction energy at a QM/MM level is the hallmark of the quantum coupling approach. The spatial partition of the entire system is shown in Fig. 1. In specific, the total energy can be expressed as

$$E_{\text{tot}}[\rho^{\text{tot}}; \mathbf{R}^{\text{tot}}] = \min_{\rho^{\text{I}}} \{E_{\text{KS}}[\rho^{\text{I}}; \mathbf{R}^{\text{I}}] + E_{\text{OF}}^{\text{int}}[\rho^{\text{I}}, \rho^{\text{II}}; \mathbf{R}^{\text{I}}, \mathbf{R}^{\text{II}}]\} + E_{\text{MM}}[\mathbf{R}^{\text{II}}] \quad (2)$$

where $\mathbf{R}^{\text{tot}} \equiv \mathbf{R}^{\text{I}} \cup \mathbf{R}^{\text{II}}$, \mathbf{R}^{I} and \mathbf{R}^{II} denote atomic coordinates in regions I and II respectively. The charge density of region I, ρ^{I} , which is the degree of freedom of the problem, is determined self-consistently by minimizing the total energy functional Eq. (2). We associate each MM atom in region II with an atomic-centered electron density (ρ^{at}) and a pseudopotential; both of them are constructed a priori and remain fixed during a QM/MM simulation. The charge density of region II, ρ^{II} , is defined as a superposition of atomic-centered charge densities ρ^{at} via $\rho^{\text{II}}(\mathbf{r}) = \sum_{i \in \text{II}} \rho^{\text{at}}(\mathbf{r} - \mathbf{R}_i)$, which only changes on the relaxation of region II ions. The total charge density ρ^{tot} is given by $\rho^{\text{tot}} = \rho^{\text{I}} + \rho^{\text{II}}$. The interaction energy between regions I and II, $E_{\text{OF}}^{\text{int}}$, formulated by orbital-free density functional theory (OF-DFT) (Garcia-Gonzalez et al., 1996; Wang and Teter, 1992; Wang et al., 1999) is defined as follows:

$$E_{\text{OF}}^{\text{int}}[\rho^{\text{I}}, \rho^{\text{II}}; \mathbf{R}^{\text{I}}, \mathbf{R}^{\text{II}}] = E_{\text{OF}}[\rho^{\text{tot}}; \mathbf{R}^{\text{tot}}] - E_{\text{OF}}[\rho^{\text{I}}; \mathbf{R}^{\text{I}}] - E_{\text{OF}}[\rho^{\text{II}}; \mathbf{R}^{\text{II}}] \quad (3)$$

The unique feature of OF-DFT is that it allows a QM calculation of energetics by knowing only the electronic density. The accuracy of OF-DFT is in between KS-DFT and EAM, which is consistent to its usage in the QM/MM method.

The plane-wave pseudopotential method implemented in the VASP package (Kresse and Furthmuller, 1996a,b) is employed for the KS-DFT simulation of region I. The KS-DFT total energy functional, $E_{\text{KS}}[\rho^{\text{I}}; \mathbf{R}^{\text{I}}]$ appearing in Eq. (2) is written as

$$E_{\text{KS}}[\{\phi\}; \{\mathbf{R}\}] = \sum_n f_n \langle \phi_n | T + V_{\text{NL}}^{\text{ion}} | \phi_n \rangle + E_{\text{H}}[\rho] + E_{\text{xc}}[\rho] + \int d\mathbf{r} V_{\text{loc}}^{\text{ion}}(\mathbf{r})\rho(\mathbf{r}) + \gamma_{\text{Ewald}}(\{\mathbf{R}\}) \quad (4)$$

where n is the index of KS orbitals ϕ_n and f_n is the occupation number. $\{\mathbf{R}\}$ denotes the position of the ions. k index is dropped for simplicity. E_{H} and E_{xc} is the Hartree energy and the exchange-correlation energy respectively. $V_{\text{loc}}^{\text{ion}}$ and $V_{\text{NL}}^{\text{ion}}$ is the local and nonlocal part of the ionic pseudopotential, respectively and γ_{Ewald} is the Madelung energy.

A similar expression can be written for OF-DFT energy functional E_{OF} as in Eq. (2), in which the electron density instead of the KS orbitals is the degree of freedom. In other words, the OF-DFT energy can be expressed as an explicit functional of electron density

$$E_{\text{OF}}[\rho; \mathbf{R}] = T_{\text{TF}}[\rho] + T_{\text{vW}}[\rho] + T_{\text{ker}}[\rho] + E_{\text{H}}[\rho] + E_{\text{xc}}[\rho] + \int d\mathbf{r} V_{\text{loc}}^{\text{ion}}(\mathbf{r})\rho(\mathbf{r}) + \gamma_{\text{Ewald}}(\{\mathbf{R}\}) \quad (5)$$

where $T_{\text{TF}} = C_{\text{TF}} \int \rho^{5/3}(\mathbf{r})d\mathbf{r}$ is the Thomas-Fermi contribution, which is exact for a uniform electron gas (Thomas, 1927; Fermi, 1928); $T_{\text{vW}} = -1/2 \int \rho^{1/2}(\mathbf{r})\nabla^2 \rho^{1/2}(\mathbf{r})d\mathbf{r}$ is the von Weizsacker term, which is exact for a single electron orbital (von Weizsacker, 1935); and $T_{\text{ker}} = \int f[\rho(\mathbf{r})](K * g)(\mathbf{r})d\mathbf{r}$ is a density-dependent convolution term to ensure the correct linear response of the electron gas (Wang et al., 1999, 2001). Here, $C_{\text{TF}} = 3/10(3\pi^2)^{2/3}$ and the convolution integral is defined as $(K * g)(\mathbf{r}) \equiv \int K(\mathbf{r} - \mathbf{r}')g(\rho(\mathbf{r}'))d\mathbf{r}'$. The three terms together represent an approximation to the exact noninteracting kinetic energy.

The minimization of total QM/MM energy [Eq. (2)] with respect to ρ^{I} leads to a self-consistent solution of the KS-like eigenvalue equations. Under the orthonormalization constrains of the KS orbitals

$$\langle \phi_n | \mathbf{S} | \phi_n \rangle = \delta_{nm} \quad (6)$$

the generalized KS eigenvalue equations become

$$\mathbf{H}|\phi_n\rangle = \epsilon_n \mathbf{S}|\phi_n\rangle \quad (7)$$

where \mathbf{S} is the overlap matrix and \mathbf{H} is the KS-like Hamiltonian given by

$$\mathbf{H} = T + V_{\text{loc}} + V_{\text{NL}} \quad (8)$$

with

$$V_{\text{loc}} = V_{\text{loc}}^{\text{ion}}[\mathbf{R}^{\text{I}}] + V_{\text{H}}[\rho^{\text{I}}] + V_{\text{xc}}[\rho^{\text{I}}] + \mu_{\text{emb}}[\rho^{\text{I}}, \rho^{\text{II}}] \quad (9)$$

where $V_{\text{H}}[\rho]$ and $V_{\text{xc}}[\rho]$ are the Hartree potential and the exchange-correlation potential, respectively. $\mu_{\text{emb}}[\rho^{\text{I}}, \rho^{\text{II}}]$ is termed embedding potential, which is defined as a functional derivative of the interaction energy $E_{\text{OF}}^{\text{int}}$ with respect to ρ^{I}

$$\mu_{\text{emb}}(\mathbf{r}) \equiv \frac{\delta E_{\text{OF}}^{\text{int}}[\rho^{\text{I}}, \rho^{\text{II}}; \mathbf{R}^{\text{I}}, \mathbf{R}^{\text{II}}]}{\delta \rho^{\text{I}}} \quad (10)$$

$\mu_{\text{emb}}(\mathbf{r})$ represents the effective single-particle potential that region I electrons feel due to the presence of region II atoms (both electrons and ions). The QM/MM coupling is achieved by including the embedding potential in the generalized KS equation; both $\mu_{\text{emb}}(\mathbf{r})$ and KS equations have to be solved self-consistently. The nonlocal potential V_{NL} depends on the total local potential V_{loc} (Kresse and Furthmuller, 1996a,b). For a given charge density ρ^{I} , one can determine the band-structure energy ϵ_n and the KS orbital ϕ_n from the KS eigenvalue equations [Eq. (7)]. And, the total energy of Eq. (2) is calculated by

$$E_{\text{tot}} = \sum_n f_n \epsilon_n + E_{\text{d.c.}} + \gamma_{\text{Ewald}}[\mathbf{R}^{\text{I}}] + E_{\text{MM}}[\mathbf{R}^{\text{II}}] \quad (11)$$

The double counting energy term $E_{\text{d.c.}}$ is given by

$$E_{\text{d.c.}} = -E_{\text{H}}[\rho^{\text{I}}] + E_{\text{xc}}[\rho^{\text{I}}] - \int d\mathbf{r} V_{\text{xc}}(\mathbf{r}) \rho^{\text{I}}(\mathbf{r}) + E_{\text{OF}}^{\text{int}}[\rho^{\text{I}}, \rho^{\text{II}}; \mathbf{R}^{\text{I}}, \mathbf{R}^{\text{II}}] - \int d\mathbf{r} \mu_{\text{emb}}(\mathbf{r}) \rho^{\text{I}}(\mathbf{r}) \quad (12)$$

Following the same numerical schemes as implemented in VASP, ρ^{I} and E_{tot} can be self-consistently determined for a given ionic configuration.

According to Eq. (5), the interaction energy and the embedding potential can be written as

$$\begin{aligned} E_{\text{OF}}^{\text{int}} &= T_{\text{TF}}^{\text{int}} + T_{\text{vW}}^{\text{int}} + T_{\text{ker}}^{\text{int}} + (E_{\text{H}}^{\text{int}} + E_{\text{e-i}}^{\text{int}} + E_{\text{i-i}}^{\text{int}}) + E_{\text{xc}}^{\text{int}} \\ \mu_{\text{emb}} &= \mu_{\text{TF}}^{\text{emb}} + \mu_{\text{vW}}^{\text{emb}} + \mu_{\text{ker}}^{\text{emb}} + \mu_{\text{H,e-i,i-i}}^{\text{emb}} + \mu_{\text{xc}}^{\text{emb}}, \end{aligned} \quad (13)$$

with various μ terms being the functional derivative of the corresponding interaction energy with respect to ρ^{I} . Here, $E_{\text{e-i}}$ and $E_{\text{i-i}}$ represent the electron-ion energy and ion-ion energy, respectively. A basic ansatz of the quantum coupling approach is that ρ^{I} must be confined within a finite volume (Ω^{I} , as shown in Fig. 1) that is necessarily larger than the volume of region I but much smaller than the entire system. In other words, ρ^{I} vanishes beyond Ω^{I} . On the other hand, there is no constrain on ρ^{II} . Ω^{I} should include region I and extend several angstroms into region II, leading to an overlap of ρ^{I} and ρ^{II} , which is a manifestation of the quantum coupling between the two regions. Thanks to the localization of ρ^{I} , there are cancellations in the evaluation of the first and third terms of Eq. (3); the cancellations ensure the calculation of $E_{\text{OF}}^{\text{int}}$ to be carried out within Ω^{I} as opposed to the entire system, as Eq. (3) appears to suggest (Choly et al., 2005; Zhang and Lu, 2007).

Here, we discuss briefly how key calculations from Eq. (7) to Eq. (13) are carried out. In the plane-wave basis, the Hamiltonian $\mathbf{H}(\mathbf{k})$ in Eq. (7) is constructed in the reciprocal space as a function of k . The local potential $V_{\text{loc}}(\mathbf{G})$, the Hartree potential $V_{\text{H}}(\mathbf{G})$ and the local pseudopotential $V_{\text{loc}}^{\text{ion}}(\mathbf{G})$ in Eq. (9) are calculated in the reciprocal space (Martin, 2004). \mathbf{G} is the reciprocal lattice vector. The exchange-correlation potential V_{xc} and the embedding potential μ_{emb} are evaluated in the real space first and then transformed into the reciprocal space by fast Fourier transformation (FFT). Once the Hamiltonian is constructed, Eq. (7) is solved in the reciprocal space. With the ground state KS orbitals, KS eigenvalues and the electron density, the total energy can be evaluated accordingly.

In the KS-DFT plane-wave calculation of region I, we introduce a periodic box Ω^{B} as shown in Fig. 1 over which the periodic boundary conditions (PBC) are imposed. The PBC are necessary for FFTs, which are crucial for efficient numerical calculations. In the following, we justify the use of the PBC with the realization that the real QM/MM system is nonperiodic. The justification is analogous to the slab model used for surface calculations with the PBC. In the slab model, the wave function and the electron density of the surface are assumed to decay exponentially so

that they are vanishing at the end of the slab vacuum. Therefore, the PBC do not lead to appreciable errors. In the QM/MM case, the basic ansatz is that ρ^I is confined within Ω^I so that the wave function and the charge density of region I decay to zero beyond Ω^I . Thus, as long as the vacuum introduced between Ω^I and Ω^B is large enough, it can effectively eliminate the fictitious interaction between the periodic images. Please note that although the PBC are also used in the present QM/MM method, the presence of the MM region provides much more realistic boundary conditions than a stand-alone periodic DFT calculation. Therefore, the QM/MM method is particularly useful for treating the extended defects, such as dislocations.

Because ρ^{II} is a key quantity for an accurate calculation of the interaction energy and the embedding potential, it is crucial to construct an appropriate representation of ρ^{II} . In fact, constructing an appropriate charge density in the MM region is a common challenge to many QM/MM methods (Lin and Truhlar, 2007). We represent ρ^{II} as a superposition of spherical atomiclike charge densities centered on each ions in region II, which is a good approximation for metallic systems. Ideally, the constructed $\rho^{II}(\mathbf{r})$ should reproduce the bulk charge density obtained by a KS-DFT calculation of the perfect lattice. That is to say, one needs to determine $\rho^{at}(r)$ by minimizing the function

$$\int_{V_u} [\rho^{II}(\mathbf{r}) - \rho^{\text{solid}}(\mathbf{r})]^2 d\mathbf{r} \quad (14)$$

with $\rho^{II}(\mathbf{r}) = \sum_{\mu} \rho^{at}(\mathbf{r} - \mathbf{R}_{\mu})$. Here V_u represents the volume of the unit cell and ρ^{solid} is the charge density obtained by a KS-DFT calculation for the perfect reference system. The summation of μ includes all the ions that have contributed to the charge density in the unit cell. For the collinear spin-polarized system, the function $\int_{V_u} [\rho^{II\uparrow}(\mathbf{r}) - \rho^{II\downarrow}(\mathbf{r}) - \rho^{\text{mag}}(\mathbf{r})]^2 d\mathbf{r}$ should also be minimized in addition to Eq. (14), where ρ^{mag} is the spin charge density calculated by KS-DFT.

We employ parametrized multiple Slater-type orbitals (MSTO) (Clementi and Rotti, 1974) for the expansion of $\rho^{at}(r)$. In MSTO, the atomic-centered charge density can be calculated as

$$\rho^{at}(r, \sigma) = \sum_i \int_{-\pi}^{\pi} \int_0^{2\pi} |c_i|^2 |\phi_i(r, \theta, \varphi, \sigma)|^2 d\theta d\varphi \quad (15)$$

where c_i is the coefficients, and the i th atomic spin orbital can be written as

$$\phi_i(r, \theta, \varphi, \sigma) = A r^{n-1} e^{-\zeta r} Y_l^m(\theta, \varphi) \sigma \quad (16)$$

where the n , l , and m are the principal, angular, and magnetic quantum number of the orbital, respectively. σ denotes the spin \uparrow or \downarrow . $Y_l^m(\theta, \varphi)$ is the spherical harmonics function, and ζ is related to the effective charge of the ion. A is the normalization constant and expressed as $A = (2\zeta)^{n+1/2} / \sqrt{(2n)!}$. The parameters of c_i and ζ can be obtained by minimizing Eq. (14) with the constraint of preserving the correct number of valence electrons.

Finally, we consider the ionic force in the present QM/MM method, which is calculated by taking the derivative of the total energy with respect to ionic displacement. At the ground state, ρ_{min}^I satisfies $\delta E_{\text{tot}} / \delta \rho_{\text{min}}^I = 0$; therefore, the ionic force in region I ($\mathbf{F}_{i \in I}$) and region II ($\mathbf{F}_{j \in II}$) can be written as

$$\begin{aligned} -\mathbf{F}_{i \in I} &= \frac{\partial E_{\text{KS}}[I]}{\partial \mathbf{R}_i} + \frac{\partial E_{\text{OF}}^{\text{int}}}{\partial \mathbf{R}_i} \\ -\mathbf{F}_{j \in II} &= \frac{\partial E_{\text{OF}}^{\text{int}}}{\partial \mathbf{R}_j} + \frac{\partial E_{\text{MM}}[II]}{\partial \mathbf{R}_j} \end{aligned} \quad (17)$$

The calculation of $-\partial E_{\text{KS}}[I] / \partial \mathbf{R}_i^I$ is carried out in the same way as implemented in VASP, and $-\partial E_{\text{MM}}[II] / \mathbf{R}_j$ can be calculated by standard MM method, such as EAM. The force contribution on the i th ion in region I due to the interaction energy is given by

$$-\mathbf{F}_{i \in I}^{\text{int}} = \frac{\partial E_{\text{OF}}^{\text{int}}}{\partial \mathbf{R}_i} = \frac{\partial [E_{\text{H}}^{\text{int}} + E_{\text{e-i}}^{\text{int}} + E_{\text{i-i}}^{\text{int}}]}{\partial \mathbf{R}_i} \quad (18)$$

The force expression on region II ions, on the other hand, is more complicated because its energy is not minimized with respect to ρ^{II} , and thus there are force contributions from the variation of ρ^{II} . The force contribution on the j th ion in region II due to the interaction energy is given by:

$$-\mathbf{F}_{j \in \text{II}}^{\text{int}} = \frac{\partial E_{\text{TF}+\text{vW}+\text{ker}}^{\text{int}}}{\partial \mathbf{R}_j} + \frac{\partial [E_{\text{H}}^{\text{int}} + E_{\text{e}-i}^{\text{int}} + E_{i-i}^{\text{int}}]}{\partial \mathbf{R}_j} + \frac{\partial E_{\text{xc}}^{\text{int}}}{\partial \mathbf{R}_j} \quad (19)$$

and the detailed expression of the various terms can be found in Zhang and Lu (2007).

For the evaluation of $\mathbf{F}_{j \in \text{II}}$, there is a disparity in the energetic formulation of $E_{\text{OF}}^{\text{int}}$ and E_{MM} . This disparity in turn leads to a disparity in force formulation, which causes coupling errors. To eliminate the coupling errors, we introduce a correction force, which is similar to a method proposed earlier by Liu et al. (2007). In this method, the force on region II ion is identical to that derived from an EAM calculation for the entire system, i.e., it becomes $\mathbf{F}_{j \in \text{II}}^* = -\partial E_{\text{MM}}[\text{I} + \text{II}]/\mathbf{R}_j$. Associated with this modification, the correction force $\Delta \mathbf{F}_{j \in \text{II}}^{\text{corr}}$ is introduced as

$$\Delta \mathbf{F}_{j \in \text{II}}^{\text{corr}} = \mathbf{F}_j^* - \mathbf{F}_j = \frac{\partial (E_{\text{OF}}^{\text{int}} - E_{\text{EAM}}^{\text{int}})}{\partial \mathbf{R}_j} \quad (20)$$

Similarly, the disparity between the KS- and OF-DFT energetic formulation also leads to coupling errors on the force of region I ions. Because $\mathbf{F}_{i \in \text{I}}^{\text{int}}$ is short range it is nonzero only for the region I ions that are adjacent to the QM/MM interface (Zhang and Lu, 2007). Therefore, the coupling errors only exist on the region I ions at the interface. We can introduce the correction force on these interface atoms in the same way as described above. In order to ensure the total energy consistent to the force which is useful for molecular dynamics simulations (Bernstein et al., 2009), we introduce the following correction to the energy as well:

$$E_{\text{tot}}^* = E_{\text{tot}} - \sum_i \Delta \mathbf{F}_i^{\text{corr}} \cdot \Delta \mathbf{R}_i \quad (21)$$

where i denotes the ion with nonzero correction force, $\Delta \mathbf{R}_i$ is the ionic displacement during the relaxation, and the last term in the equation represents the work done by the correction force. The correction force method has been shown to significantly reduce the force coupling errors (Zhang and Lu, 2007; Liu et al., 2007).

2.2 Mechanical Coupling

In the mechanical coupling, the interaction energy E^{int} is evaluated with MM calculations

$$E^{\text{int}}[\text{I}, \text{II}] = E_{\text{MM}}[\text{I} + \text{II}] - E_{\text{MM}}[\text{I}] - E_{\text{MM}}[\text{II}] \quad (22)$$

and, thus, Eq. (2) becomes

$$E_{\text{tot}}[\text{I} + \text{II}] = E_{\text{KS}}[\text{I}] + E_{\text{MM}}[\text{I} + \text{II}] - E_{\text{MM}}[\text{I}] \quad (23)$$

and the atomic forces can be derived as

$$-\mathbf{F}_i = \frac{\partial E_{\text{KS}}[\text{I}]}{\partial \mathbf{R}_i} + \frac{\partial E_{\text{MM}}[\text{I} + \text{II}]}{\partial \mathbf{R}_i} - \frac{\partial E_{\text{MM}}[\text{I}]}{\partial \mathbf{R}_i} \quad (24)$$

The QM/MM approach can be interpreted as applying the QM correction to the MM description of region I because MM itself is not considered accurate enough for region I (Svensson et al., 1996). A major practical advantage of this approach is that, if region I contains many different atomic species while region II contains only one atom type, then there is no need to have a classical potential for each species and their interactions. This results from the fact that if the various species of atoms are well within region I, then the energy contributions of these atoms cancel out in the total energy calculation [the last two terms in Eq. (23)]. Thus, this coupling approach is particularly useful in dealing with impurities, which is an exceedingly difficult task for classical simulations.

In the mechanical coupling, we focus on the calculation of atomic force and try to minimize the coupling errors in the force calculations (Solt et al., 2009). As shown in Fig. 2(a), the computational model is divided into region I and II

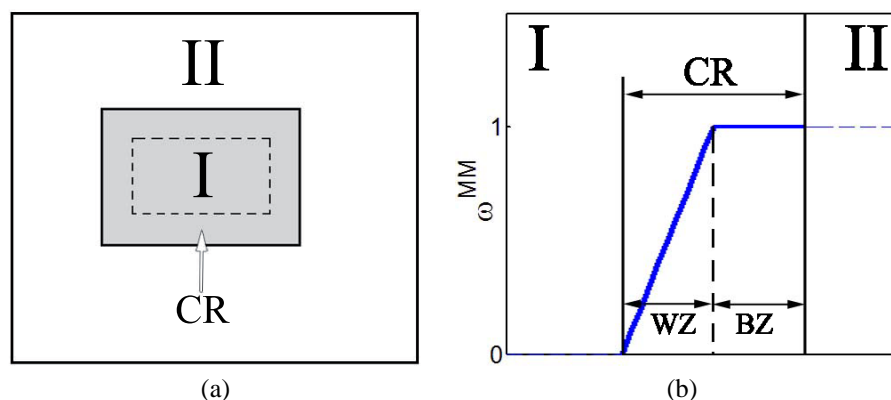


FIG. 2: (a) Schematic partition of a QM/MM system into region I (in gray) and region II. The region I is further subdivided into an inner region (dashed box) and a coupling region (CR). (b) The form of the weighting function ω^{MM} in relation to the weighted zone and the buffer zone.

as usual. However, region I is sub-divided into an inner region (within the dashed box) and a so-called coupling region (CR). For the DFT atoms in the inner region, the atomic force is calculated according to Eq. (24). In the coupling region, however, the atomic force, $\mathbf{F}_i^{\text{QM/MM}}$ is calculated as

$$\mathbf{F}_i^{\text{QM/MM}} = \omega^{\text{MM}} \mathbf{F}_i^{\text{MM}} + (1 - \omega^{\text{MM}}) \mathbf{F}_i \quad (25)$$

where $\mathbf{F}_i^{\text{MM}} = -\partial E_{\text{MM}}[\text{I} + \text{II}]/\partial \mathbf{R}_i$ and \mathbf{F}_i is given in Eq. (24). The weighting function (Kerdcharoen et al., 1996) ω^{MM} is defined in CR only and the form of ω^{MM} is shown in Fig. 2(b). Furthermore, the CR could consist of two parts: (i) A “buffer zone” (BZ) in which $\omega^{\text{MM}} = 1$ (the purpose of BZ is to reduce the fictitious surface effect from the DFT cluster calculation of region I) and (ii) a linearly weighted zone (WZ) which smoothes the mixture of QM and MM forces. Comparing Eqs. (24) and (25), one can derive the correction force in CR as

$$\mathbf{F}_i^{\text{corr}} = \mathbf{F}_i^{\text{QM/MM}} - \mathbf{F}_i = \omega^{\text{MM}} (\mathbf{F}_i^{\text{MM}}[\text{I}] - \mathbf{F}_i^{\text{QM}}[\text{I}]) \quad (26)$$

where $\mathbf{F}_i^{\text{QM}}[\text{I}] = -\partial E_{\text{KS}}[\text{I}]/\partial \mathbf{R}_i$ is the QM force in region I. Because of the correction, the force $\mathbf{F}_i^{\text{QM/MM}}$ is no longer the derivative of the total energy as defined in Eq. (23). This inconsistency could lead to problems in atomic relaxation and more seriously in molecular dynamics simulations. Therefore, a correction energy which is the work done by the correction force should be added to the original total energy expression

$$E_{\text{corr}} = \sum_{i \in \text{CR}} \int \mathbf{F}_i^{\text{corr}} \cdot d\mathbf{R}_i \quad (27)$$

$$E' = E_{\text{tot}}[\text{I} + \text{II}] + E_{\text{corr}}$$

where E' is the corrected total energy used in atomic relaxation and/or molecular dynamics.

3. VALIDATION

3.1 Quantum Coupling

Central to the quantum coupling approach is the embedding potential, which represents the physical effect that electrons in region I feel due to the presence of region II. Without the embedding potential, ρ^{I} will correspond to the charge density of a bare cluster. The presence of the embedding potential is thus to remove the fictitious surface states

and render a realistic description of ρ^I . In this section, we take Al as an example to validate the quantum coupling approach. The test model is a perfect lattice of Al containing $14a_0 \times 14a_0 \times a_0$ ($a_0 = 3.983\text{\AA}$ is the lattice constant of Al) as the entire system with the innermost $3.5a_0 \times 3.5a_0 \times a_0$ as region I. The distance that ρ^I extends to region II is 2.61\AA , and the size of the periodic box is $8a_0 \times 8a_0 \times a_0$. First, the behavior of the embedding potential is presented. Then, we perform a critical assessment of the influence of embedding potential on the total electronic density and electronic states at the Fermi energy of the primary quantum system. Finally, the structural optimization by the quantum coupling approach is examined.

Figure 3(a) presents the total local potential of the system, the local potential of region I and the embedding potential. All these potentials are defined with respect to ρ^I . The total local potential consists of the local potential of region I and the embedding potential as shown in Eq. (9); the first three terms on the right-hand side of the equation represents the local potential of region I. In Figs. 3(b) and 3(c), we show the charge density ρ^I and ρ^{II} , respectively. First of all, all potentials vanish beyond Ω^I due to the constraint imposed on the total local potential. This constraint has successfully enforced ρ^I to be zero beyond Ω^I , as shown in Fig. 3(b). ρ^I and ρ^{II} only overlap over a distance (around $0.5a_0$) where the embedding potential is nonzero. The fact that ρ^I and ρ^{II} overlap is of crucial importance and the result of the self-consistent quantum mechanical coupling. The sum of both densities should give the correct total density of the system. From Fig. 3, it is observed that the embedding potential is localized at the QM/MM interface and decays to zero in the interior of region I. The behavior of the total local potential at the interface is different from that at the interior of region I; this is because the total local potential is defined with respect to ρ^I , which is equal to ρ^{tot} only at the interior of region I but not at the interface. Once the total local potential associated with ρ^{II} is included, the total local potential will be periodic throughout the entire space for the perfect lattice.

Next, we examine the results of total electron density by the quantum coupling approach. In the following, we refer the calculations using the quantum coupling approach as embedding calculations. For comparisons, we also perform two different calculations: (i) bulk—where region I is treated by a stand-alone KS-DFT calculation with periodic boundary conditions; (ii) vacuum—where region I is treated by a stand-alone KS-DFT calculation as a bare cluster. If the embedding scheme worked perfectly, then the embedding calculation would reproduce the same results of the bulk

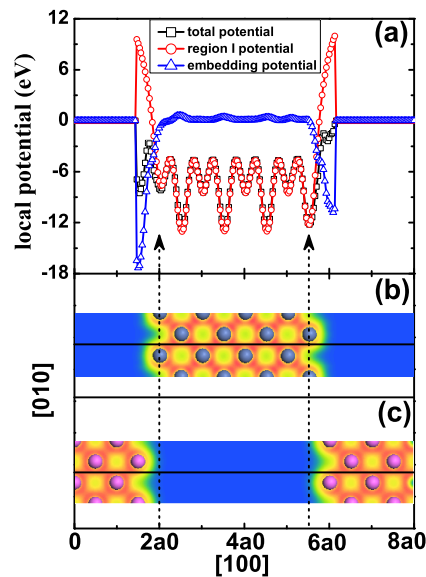


FIG. 3: (a) Total local potential, local potential in region I and the embedding potential are plotted along a straight line in [100] direction for a perfect Al system. The position of the straight horizontal line is indicated in (b) and (c). Charge density ρ^I and ρ^{II} in $x - y$ plane are plotted in (b) and (c), respectively. The blue (magenta) spheres represent the region I (II) ions, and the contour scale (in \AA^{-3}) ranges from 0.0 (blue) to 0.225 (red).

calculation for the perfect lattice model. The vacuum calculation correspond to $E_{\text{KS}}[\text{I}]$ of Eq. (23) in the mechanical coupling. As shown in Figs. 4(a), 4(b), and 4(d), there is a rather good agreement of the total charge density between the bulk and the embedding calculations. The minor density errors at the interface are due to (i) the disparity in the energy functional between KS- and OF-DFT, and (ii) the first that the superposition of the atomic-centered charge densities do not reproduce the bulk charge density exactly. On the other hand, as expected, the total charge density of the vacuum calculation shown in Fig. 4(c) differs significantly from the bulk result, with the greatest errors occurring at the surfaces. Specifically, the surface charge density does not resemble the directional bonding that exists in bulk Al (Zhang and Lu, 2007). In Fig. 4(e), we plot the differential charge density between the embedding and the vacuum calculation for region I, $\rho_{\text{embed}}^{\text{I}}(\mathbf{r}) - \rho_{\text{vacuum}}^{\text{I}}(\mathbf{r})$. It is evident that the charge density difference is primarily localized at the QM/MM interface, and it is due to the nearest-neighbor directional bonding. Therefore, the embedding potential can reproduce the directional bonding that is characteristic of bulk Al.

Next, we analyze the band-decomposed charge density to examine the effect of the embedding potential on the electronic states near the Fermi energy. The band-decomposed charge density at E_{F}^{-} and E_{F}^{+} for the vacuum and the embedding calculations are presented in Figs. 5(a) and 5(b), respectively. Here, the band-decomposed charge density at E_{F}^{-} (E_{F}^{+}) is evaluated in the energy range between $E_{\text{F}} - 0.1$ eV and E_{F} (E_{F} and $E_{\text{F}} + 0.1$ eV), including the contributions of all k points. We focus on these states because they constitute possible “frontier orbitals” and could play critical roles in chemical reactions for certain material systems. It turns out that the majority contributions to the band-decomposed charge density at E_{F}^{-} come from the surface atoms in the vacuum calculation; the electronic states at E_{F}^{-} are mainly localized surface states. On the other hand, the electronic states at E_{F}^{+} are much more extended and spread all over the primary region. Although the surface states are clearly visible in Fig. 5(a) of the vacuum calculation, they are significantly suppressed by the embedding potential as shown in Fig. 5(b). As expected, the short-range embedding potential has little effect on the extended states at E_{F}^{+} ; there is minor difference between Figs. 5(a) and 5(b) in terms of E_{F}^{+} states. Therefore, the embedding potential could suppress or eliminate the localized surface states arising from the vacuum calculation but has little effect on the extended states that are inherent to the bulk system. For

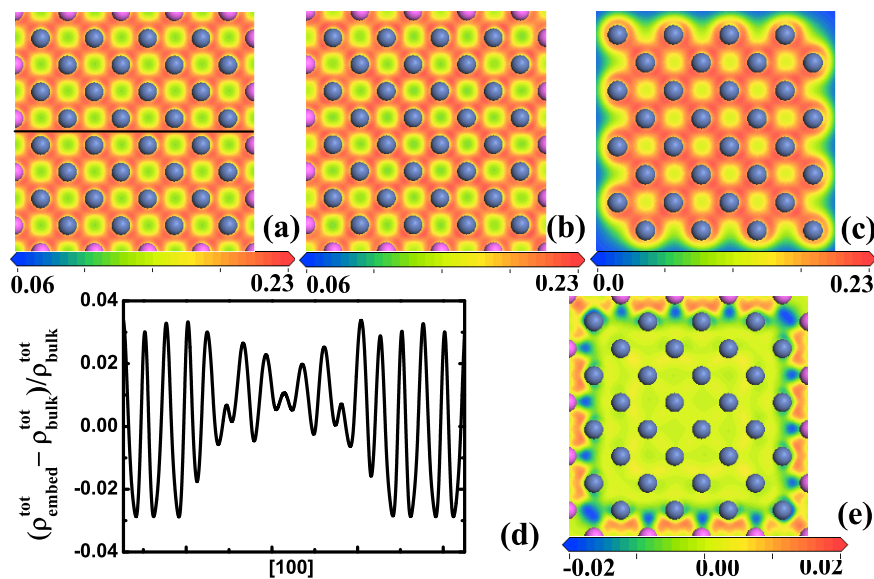


FIG. 4: Total charge density (\AA^{-3}) in the primary region from: (a) the bulk calculation, (b) the embedding calculation, and (c) the vacuum calculation. (d) The difference of the total charge density between the embedding and the bulk calculations along a horizontal line shown in (a). The difference is normalized with respect to the bulk values. (e) The difference of the charge density ρ^{I} between the embedding and the vacuum calculations. The blue and magenta (partially visible) spheres represent region I and II atoms, respectively.

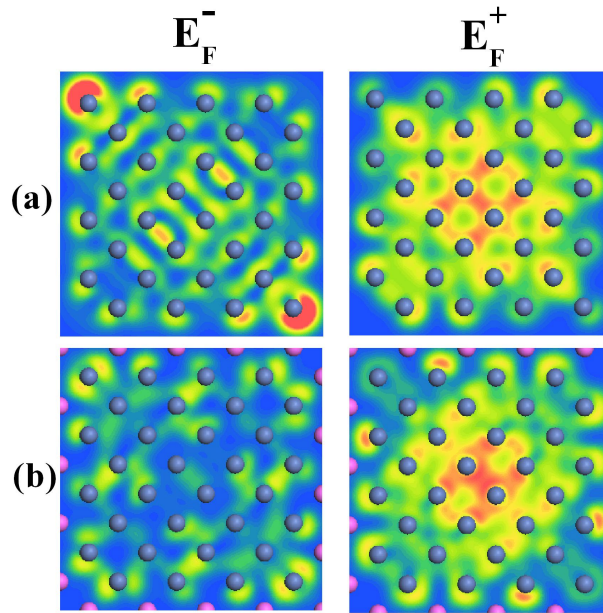


FIG. 5: Band-decomposed charge density at E_F^- and E_F^+ (a) the vacuum calculation, (b) the embedding calculation. Contour scale (in \AA^{-3}) ranges from 0.0 (blue) to 0.007 (red). The blue and magenta (partially visible) spheres represent region I and II atoms, respectively.

systems with defects, the quantum coupling approach is useful because, no matter how large a bare cluster is chosen for a QM calculation, the surface states are always present and show up close to the Fermi energy as frontier orbitals. These fictitious states can be eliminated by a moderate size embedding calculation. On the other hand, the fictitious surface states cannot be suppressed or removed by mechanical coupling approaches even though these approaches are capable of predicting reliable atomic structures.

Finally, we examine the coupling errors of the quantum coupling approach in terms of atomic structure optimization. If the QM/MM coupling were perfect, then the force and displacement on each ion in the perfect lattice would be identically zero because regions I and II have the same lattice constant. In other words, any nonzero force or displacement is indicative of coupling errors. One can thus estimate the coupling errors by examining the magnitude of force/displacement on each ion in the test system. We denote F_{\max}^I (F_{\max}^{II}) as the maximum force on region I (II) atoms, and d_{\max}^I (d_{\max}^{II}) as the maximum displacement on region I (II) atoms, respectively. The correction forces are applied on the region II atoms, and the relaxation for all ions is performed until the maximum force on any ion is < 0.01 eV/ \AA . The evaluated F_{\max}^I , F_{\max}^{II} , d_{\max}^I , and d_{\max}^{II} are 0.065 eV/ \AA , 0.0 eV/ \AA , 0.009 \AA , and 0.004 \AA , respectively. It is observed that the correction force has essentially eliminated the coupling errors for region II atoms. Therefore, the quantum coupling approach can obtain very reliable results in terms of atomic structure.

3.2 Mechanical Coupling

One of the critical requirements for a QM/MM approach is that the QM/MM interface should be transparent; it shall not introduce any discontinuities. This requirement is often more rigorous in a molecular dynamics (MD) simulation than in a static relaxation. For MD, one has to insist that the same thermal conductivity be maintained across the interface so that the lattice vibrations are not impinged or reflected in a nonphysical way.

First, the QM/MM approach is tested in static atomic relaxation for a Au thin film. The thickness of the Au film along the Z direction is 160 \AA with the open boundary. The system measures 4.06 \AA in the X and Y directions along which the PBC are applied. The region I with a thickness of 30 \AA is placed in the middle of the computational model

along the Z direction as shown in Fig. 6(a). A DFT-based tight-binding (TB) model (Bernstein et al., 2000) is used to describe region I, and EAM is used for the region II. The EAM potential is scaled to match the lattice constant and bulk modulus of the corresponding TB values. The test is carried out with different sizes of CR and WZ. The deviations from the ideal equilibrium atomic position are considered as the coupling errors. It is found that the errors decrease significantly as the size of CR increases, but the width of WZ plays a minor role as demonstrated in Fig. 7(a). The variation of the energetics during the relaxation is shown in Fig. 7(b), and the corrected total energy is appropriately minimized.

MD simulations are also carried out for this system to check the energy conservation. A larger 3×3 supercell is used along the X and Y directions, and PBC is applied in the Z direction. The initial velocities are assigned to the atoms according to the Maxwell distribution at 300 K; the atomic velocities and positions are updated via the Verlet algorithm with no thermostat applied. The variation of the energetics is shown in Fig. 7(c). In a short-time interval, the total energy is conserved to a good accuracy thanks to the contribution of E_{corr} . During a longer time interval, the total energy is drifted on the order of 1×10^{-3} eV per atom; the energy change is due to the fact that the integral in Eq. (27) is path-dependent, and thus, the total energy is not strictly conservative. Overall, however, the correction force/energy is a reasonable approximation that can effectively conserve the energy and reduce the coupling errors.

Another test is performed to examine the transparency of the QM/MM interface to lattice vibrations. Si and Au thin films are simulated with the computational setup similar to the static relaxation except that the region I is placed at the left end of the system. The schematic partition of the computational model is shown in Fig. 6(b). Both longitudinal

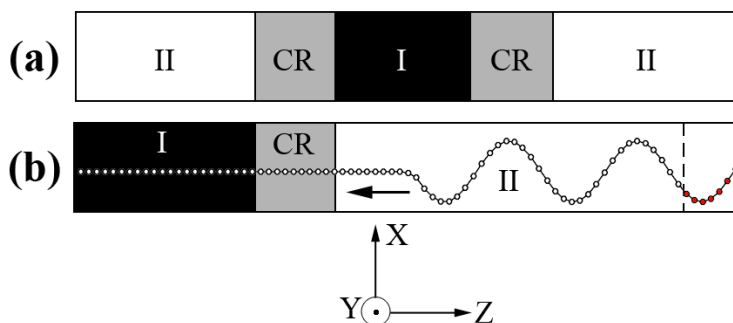


FIG. 6: Schematic partition of the computational model: (a) static relaxation and (b) MD simulation. The atoms are shown in circles. The lattice vibrations are introduced from the right end of the model, represented by the red circles.

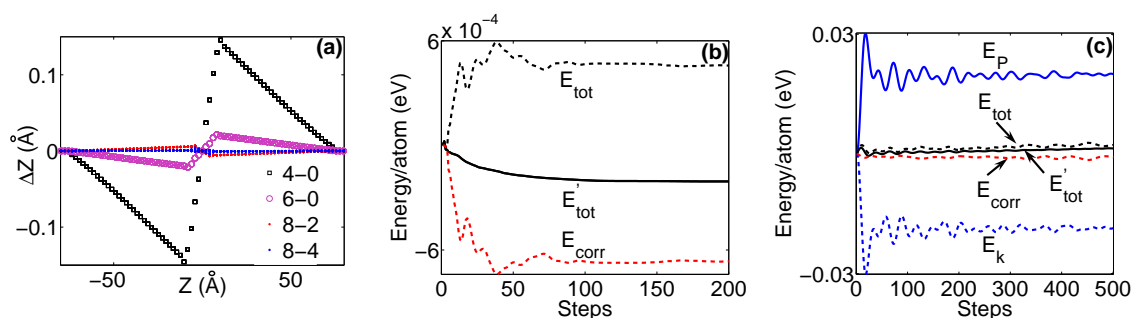


FIG. 7: (a) Atomic displacement as a function of the Z coordinate for different choices of CR and WZ size. The first and second number refers to the size of CR and WZ in terms of the lattice constant a_0 . (b) energy variation in the static relaxation as a function of iteration step. (c) energy variation in the MD simulations as a function of time step. The energy is set to zero at $t = 0$. E'_{tot} and E_{tot} are the total energy with and without the correction respectively; E_P is the potential energy without the correction; E_{corr} is the correction energy, and E_K is the kinetic energy.

or transverse lattice vibrations are introduced from the right end of the model and propagate toward the region I. The amplitude of the waves is 0.3 \AA , and the driving frequency is $3 \times 10^{12} \text{ Hz}$. After the vibrational waves propagate into the region I, the reflected waves, if any, will overlap with the incident waves and result in a change of wave profile. Thus, the interfacial transparency may be evaluated by the change of the wave amplitude. The test results for both Si and Au are summarized in Fig. 8. The change of the wave amplitude is measured as a function of the CR and BZ size. It is shown that the width of CR is again the critical factor affecting the transparency. This width is more critical for Au comparing to Si. This difference is due to the delocalized electronic states and longer range atomic interactions in Au comparing to Si. In addition, it is found that the required size of CR is larger for the longitudinal wave than for the transverse wave due to the fact that the longitudinal vibrations are in the same direction of the force errors.

4. APPLICATIONS

4.1 Quantum Coupling

We have employed the quantum coupling approach to calculate the binding energy of vacancy clusters in Al (Zhang and Lu, 2008). Although ab initio calculations have been performed for small vacancy clusters in Al (Carling et al., 2003), little effort has been devoted to QM calculations of relatively larger vacancy clusters, which are the key to understanding void formation in materials. By using the QM/MM approach, we are able to carry out large scale calculations consisting of up to 10-vacancy in a cluster. The results of binding energy are shown in Fig. 9. The binding energy of a divacancy in Al from the quantum coupling approach is -0.08 eV , which is identical to the value obtained from a stand-alone KS-DFT calculation (Carling et al., 2003). In addition, we find there is a charge accumulation (or a bonding ring) formed between the atoms in the first shell around the vacancy (see inset of Fig. 9). This vacancy-induced circular bonding has also been observed by others from stand-alone KS-DFT calculations (Carling et al., 2003). The comparisons here suggest that the present quantum coupling approach reproduces the stand-alone KS-DFT results, a validation of the coupling method.

We also used the quantum coupling approach to simulate the core structure of an edge dislocation in Al (Zhang and Lu, 2010). In fcc metals, dislocations can reduce the elastic energy by separating into Shockley partials connected by a stacking fault. For materials with large stacking fault energies, such as Al, the separation distance between two partials can be quite narrow, making experimental investigation of the core structure difficult (Mills et al., 1994). An accurate

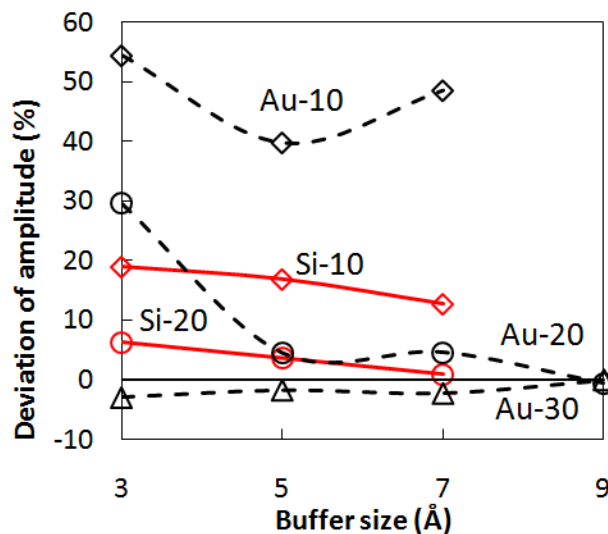


FIG. 8: Maximum deviation of the vibrational amplitude measured as a functional of BZ size. Caption "Si-2" refers to the system of Si and the width of CR is $2a_0$.

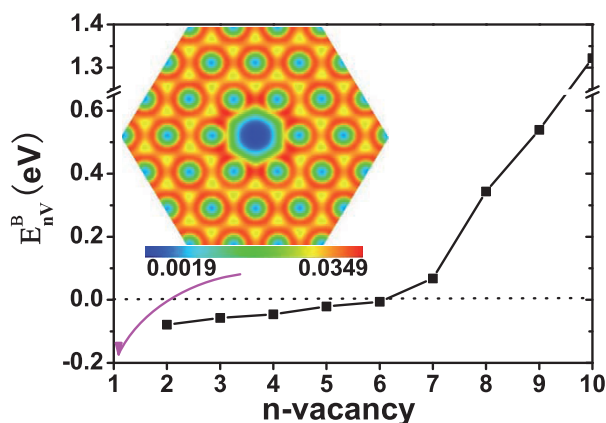


FIG. 9: Binding energy (eV) of n -vacancy clusters versus number n . Inset: Bonding charge density (\AA^{-3}) in a close-packed $\{111\}$ plane in the presence of a monovacancy. The bonding charge density is defined as the difference between the total solid density and the superposition of atomic densities centered at all atoms.

simulation of dislocations is challenging due to the following reasons: (i) In order to capture the severe deformation and possible bond breaking at the dislocation core, quantum mechanical calculations are often required. (ii) Standard ab initio quantum mechanical calculations employ either the PBC or open boundary conditions (OBC). Neither of them is satisfactory. The PBC lead to fictitious interaction among dislocation images and the fact the dislocations dissociate into partials render the problem even worse. The OBC involve fictitious interaction between the dislocation and surface. The quantum coupling approach can treat the core region quantum mechanically by coupling to the long-range elastic distortion beyond the core. Figure 10 shows the dislocation density and core structure. We find that the partial separation distance is 7\AA , which agrees very well to the experimental measurements from the weak-beam transmission electron microscopy of 8\AA (Hollerbauer and Karnthaler, 1981). The quantum coupling method has also been used to study dislocation pipe diffusion in Al (Zhang and Lu, 2010).

In conjunction with the quasi-continuum (QC) method (Tadmor, 1996), the quantum coupling approach has been implemented in QC to simulate 60 million atoms effectively via the density functional theory (Peng et al., 2008). The multiscale method is used to examine the solid solution effect on dislocation nucleation during nanoindentation in Al. Because the load-displacement curve is the typical observable for nanoindentation and is widely used both experimentally and theoretically, we have calculated the load-displacement curves using the multiscale method. In particular, it is conventional to identify the onset of incipient plasticity with the first drop in the load-displacement curve during indentation. Figure 11 shows the computed load-displacement curves of an Al thin film with Mg impurities (Peng et al., 2010). The results reveal that Mg impurities can strengthen the hardness of Al and hinder the dislocation nucleation. Consistent with experimental results on Ni/Cu alloys, the extent of the solid solution strengthening is found to be small, of the same order of magnitude of the change in shear modulus. The results suggest that the quantum coupling based QC approach is a promising method for quantum simulations of material properties at length scales relevant to experiments.

4.2 Mechanical Coupling

Fracture is a typical material problem that has been widely studied using multiscale approaches (Kohlhoff et al., 1991; Bernstein and Hess, 2003; Csanyi et al., 2004; Buehler et al., 2007). First, the mechanical coupling method is used to simulate fractures in Si. In this case, a quantum mechanical DFT-based tight-binding (TB) method is coupled to the empirical Stillinger-Webber (SW) potential (Stillinger and Weber, 1985). Four types of mode I cracks were simulated: $\{110\}\langle 001\rangle$, $\{110\}\langle 110\rangle$, $\{111\}\langle 110\rangle$, and $\{111\}\langle 112\rangle$. Hereafter, the crack with $\{110\}$ cleavage plane propagating along $\langle 001\rangle$ direction is abbreviated as $\{110\}\langle 001\rangle$. A plane strain field (Becquart et al., 1993; Mara et al., 1990) is

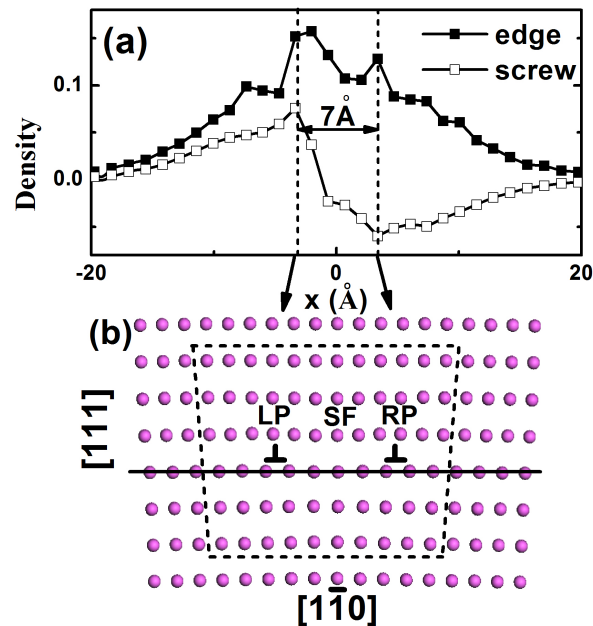


FIG. 10: (a) Edge and screw component of the displacement density as a function of x . The double peak in the density plot illustrates the dissociation of the perfect edge dislocation into two Shockley partials. The distance between the two partials is 7 Å. (b) The atomic structure of the edge dislocation (partially shown) on $(11\bar{2})$ plane. LP and RP represent the left and right Shockley partial, respectively and the stacking fault ribbon is denoted as SF between the partials. The atoms within the dash box are treated by DFT, and the others are treated by EAM. The magenta spheres represent Al atoms.

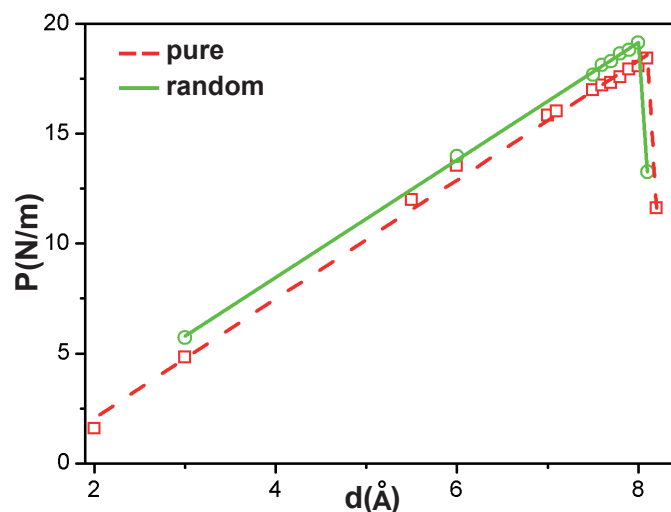


FIG. 11: Load vs. displacement plot for the nanoindentation of the Al thin film with a rigid rectangular indenter: pure Al (red squares) and randomly distributed Mg impurity system (green circles). The corresponding lines are the best fit to the computational data points.

applied to generate the initial crack structures. The mode I critical loading is given in terms of the energy release rate following the Griffith criterion, G_c . The QM/MM molecular dynamics simulations are carried out at a temperature of 300 K. For the $\{110\}\langle 001\rangle$ crack, both QM/MM and the stand-alone SW molecular dynamics simulations predict that the crack will change to $\{111\}\langle 112\rangle$. For the other three types of cracks (see Fig. 12 for an example) the QM/MM method predicts brittle behavior of the crack which propagates with flat cleavage surfaces. In a strong contrast, the stand-alone SW simulations show either no crack propagation or a much lower propagation speed. More importantly, the crack tip appears to be always blunted. Our results reinforce the well-known fact that empirical potentials cannot treat brittle fracture accurately.

The mechanical coupling is also applied to study the fracture in metals. For example, the TB method is coupled to EAM to simulate ductile fracture in Au. The EAM potential is scaled to match the lattice constant and bulk modulus from the corresponding TB values (Johnson, 1998). We find that the Griffith stress intensity for crack propagation is $K_{IC} = \sqrt{2\gamma E} = 0.39 \text{ eV}/\text{\AA}^{2.5}$. Here, 2γ is twice the surface energy and E is Young's modulus, whose TB values are 2.97 J/m^2 and 128 GPa , respectively. Both QM/MM and stand-alone EAM method predict a ductile behavior in which dislocations are emitted from the crack tip. In specific, QM/MM predicts that at a critical load of $K_I = 0.10 \text{ eV}/\text{\AA}^{2.5}$, dislocations are nucleated at the crack tip and moved to the MM region across the QM/MM interface. This implies that the coupling interface is transparent for dislocation transmission. On the other hand, the stand-alone EAM simulations find a higher critical stress intensity at $0.122 \text{ eV}/\text{\AA}^{2.5}$.

Finally, the mechanical coupling has been used to explore the interplay between magnetism and dislocation properties in NiAl. In this case, a plane-wave pseudopotential DFT method implemented in VASP (Kresse and Furthmuller, 1996a,b) is coupled to EAM. The screw dislocation with the Burgers vector $[001]$, which plays a central role in the plastic deformation of NiAl is studied. The first-principles DFT-based QM/MM calculations show that by substituting Ni atom at the dislocation core, Fe and Co impurities can lead to spontaneous dislocation cross-slip, show in Fig. 13.

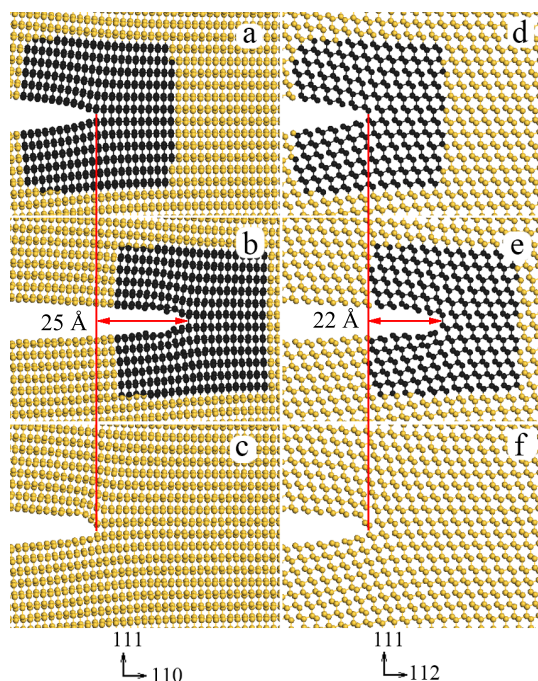


FIG. 12: Simulations of Si $\{111\}\langle 100\rangle$ (left column) and $\{111\}\langle 112\rangle$ (right column) cracks under loading of $1.5 G_c$. Upper row, initial structures, and region I atoms are in black and region II atoms in gold; middle row, after 1.5 ps simulated by the QM/MM method; the arrow indicates the distance that the crack tip has traveled; bottom row, after 1.5 ps simulated by the MM method; the cracks do not propagate.

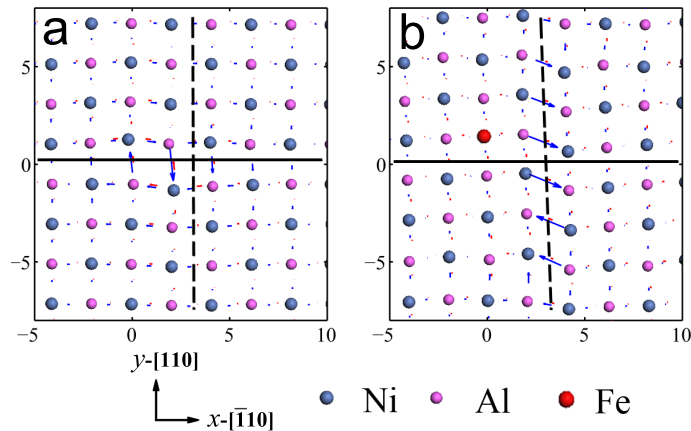


FIG. 13: Differential displacement field plot of the dislocation. (a) Pure system: the screw displacement is shown in blue. The magnitude of the displacement is proportional to the length of the arrow. The solid and dashed line indicate the primary and cross-slip plane, respectively. The horizontal and vertical axis (in Å) correspond to the x and y directions, respectively. (b) The displacement field of the impurity system.

In the absence of the impurity, the dislocation core spreads over the horizontal slip plane (110); when the Fe impurity is introduced at the dislocation core, the dislocation spontaneously cross-slips to the vertical cross-slip plane ($\bar{1}10$). For the Fe impurity on Al site, we find that the Peierls stress for the dislocation in the absence and presence of the impurity is 900 and 600 MPa, respectively. Thus, the dislocation mobility is increased significantly; this is consistent with the experimental observation that Fe can reduce the hardness of Ni-rich NiAl (Savage et al., 1998). The enhanced dislocation mobility appears to be magnetism driven. When the spin-polarization is turned off in the DFT calculation, the dislocation core narrows and cross-slips to the ($\bar{1}10$) plane. The QM/MM calculations unambiguously demonstrate the connections between magnetism and the mechanical properties of NiAl alloys.

5. CONCLUSION

We have introduced two QM/MM approaches: one is based on the quantum mechanical coupling and the other on the mechanical coupling. The formalism of both approaches is described in detail. The validations of the methods are demonstrated in terms of atomic and electronic structure. Finally the applications of the methods are surveyed, including applications in vacancy clusters, dislocations, nanoindentations and fractures.

ACKNOWLEDGMENTS

This work was supported in part by NSF Grant No. DMR-0611562 and ONR Grant No. N00014-11-1-0175.

REFERENCES

- Becquart, C. S., Kim, D., Rifkin, J. A., and Clapp, P. C., Fracture properties of metals and alloys from molecular-dynamics simulations, *Mater. Sci. Eng. A*, vol. **170**, no. 1–2, pp. 87–94, 1993.
- Bernstein, N., Mehl, M. J., Papaconstantopoulos, D. A., Papanicolaou, N. I., Bazant, M. Z., and Kaxiras, E., Energetic, vibrational, and electronic properties of silicon using a nonorthogonal tight-binding model, *Phys. Rev. B*, vol. **62**, no. 7, pp. 4477–4487, 2000.
- Bernstein, N. and Hess, D. W., Lattice trapping barriers to brittle fracture, *Phys. Rev. Lett.*, **91**, no. 2, p. 025501, 2003.
- Bernstein, N., Kermode, J. R., and Csanyi, G., Hybrid atomistic simulation methods for materials systems, *Rep. Prog. Phys.*, vol. **72**, no. 2, p. 026501, 2009.

- Buehler, M. J., Tang, H., van Duin, A. C. T., and Goddard III, W. A., Threshold crack speed controls dynamical fracture of silicon single crystals, *Phys. Rev. Lett.*, vol. **99**, no. 16, p. 165502, 2007.
- Carling, K., Wahnström, G., Mattsson, T., Sandberg, N., and Grimvall, G., Vacancy concentration in Al from combined first-principles and model potential calculations, *Phys. Rev. B*, vol. **67**, no. 5, p. 054101, 2003.
- Choly, N., Lu, G., E, W., and Kaxiras, E., Multiscale simulations in simple metals: A Density-functional-based methodology, *Phys. Rev. B*, vol. **71**, no. 9, p. 094101, 2005.
- Clementi, E. and Rotti, C., *Atomic Data and Nuclear Data Tables*, vol. **14**, Nos. 3 and 4, New York, Academic Press, 1974.
- Csányi, G., Albaret, T., Payne, M. C., and DeVita, A., Learn on the fly: A hybrid classical and quantum-mechanical molecular dynamics simulation, *Phys. Rev. Lett.*, vol. **93**, no. 17, p. 175503, 2004.
- Daw, M. S. and Baskes, M. I., Embedded-atom method—derivation and application to impurities, surfaces, and other defects in metals, *Phys. Rev. B*, vol. **29**, no. 12, pp. 6443–6453, 1984.
- Fermi, E., Eine statistische methode zur bestimmung einiger eigenschaften des atoms und ihre anwendung auf die theorie des periodischen systems der elemente *Z. Phys.*, vol. **48**, pp. 73–79, 1928.
- Gao, J. L. and Truhlar, D. G., Quantum mechanical methods for enzyme kinetics, *Annu. Rev. Phys. Chem.*, vol. **53**, pp. 467–505, 2002.
- GarciaGonzalez, P., Alvarillos, J. E., and Chacon, E., Nonlocal kinetic-energy-density functionals, *Phys. Rev. B*, vol. **53**, no. 15, pp. 9509–9512, 1996.
- Höllerbauer, W. and Karthaler, H. P., *Beitr. Elektronenmikroskop. Direktabb. Oberfl.*, vol. **14**, p. 361, 1981.
- Johnson, R. A., Analytic nearest-neighbor model for fcc metals, *Phys. Rev. B*, vol. **37**, no. 8, pp. 3924–3931, 1988.
- Kerdcharoen, T., Liedl, K. R., and Rode, B. M., A Qm/mm simulation method applied to the solution of Li+ in liquid ammonia, *Chem. Phys.*, vol. **211**, no. 1–3, pp. 313–323, 1996.
- Kohlhoff, S., Gumbsch, P., and Fischmeister, H. F., Crack-propagation in bcc crystals studied with a combined finite-element and atomistic model, *Phil. Mag. A*, vol. **64**, no. 4, pp. 851–878, 1991.
- Kohn, W. and Sham, L. J., Self-consistent equations including exchange and correlation effects, *Phys. Rev.*, vol. **140**, no. 4A, pp. 1133–1138, 1965.
- Kresse, G. and Furthmüller, J., Efficient iterative schemes for ab initio total-energy calculations using a plane-wave basis set, *Phys. Rev. B*, vol. **54**, no. 16, pp. 11169–11186, 1996a.
- Kresse, G. and Furthmüller, J., Efficiency of ab-initio total energy calculations for metals and semiconductors using a plane-wave basis set, *Comput. Mat. Sci.*, vol. **6**, no. 1, pp. 15–50, 1996b.
- Lin, H. and Truhlar, D. G., QM/MM: what have we learned, where are we, and where do we go from here?, *Theor. Chem. Acc.*, vol. **117**, no. 2, pp. 185–199, 2007.
- Liu, Y., Lu, G., Chen, Z. Z., and Kioussis, N., An improved QM/MM approach for metals, *Modelling Simul. Mater. Sci. Eng.*, vol. **15**, no. 3, pp. 275–284, 2007.
- Lu, G. and Kaxiras, E., *Handbook of Theoretical and Computational Nanotechnology*, Stevenson Ranch: American Scientific, Chap. 22, 2004.
- Mara, W. C., Herring, R. B., and Hunt, L. P., *Handbook of Semiconductor Silicon Technology*, Noyes Publications, Park Ridge, New Jersey, 1990.
- Martin, R. M., *Electronic Structure: Basic Theory and Practical Methods*, Cambridge University Press, Cambridge, Section 12, 2004.
- Mills, M. J., Daw, M.S., and Foiles, S. M., High-resolution transmission electron-microscopy studies of dislocation cores in metals and intermetallic compounds, *Ultramicroscopy*, vol. **56**, no. 1–3, pp. 79–93, 1994.
- Mordasini, T. and Thiel, W., Combined quantum mechanical and molecular mechanical approaches, *Chimia*, vol. **52**, no. 6, pp. 288–291, 1998.
- Peng, Q., Zhang, X., Hung, L., Carter, E. A., and Lu, G., Quantum simulation of materials at micron scales and beyond, *Phys. Rev. B*, vol. **78**, no. 5, p. 054118, 2008.
- Peng, Q., Zhang, X., and Lu, G., Quantum mechanical simulations of nanoindentation of Al thin film, *Comput. Mater. Sci.*, vol. **47**, no. 3, pp. 769–774, 2010.
- Savage, M. F., Srinivasan, R., Daw, M. S., Lograsso, T., and Mills, M. J., Dislocation processes and deformation behavior in (Fe,Ni)-Al single crystals, *Mater. Sci. Eng. A*, vol. **258**, no. 1-2, pp. 20–25, 1998.
- Sherwood, P., *Modern methods and algorithms of quantum chemistry*, NIC-Directors: Princeton, pp. 285–305, 2000.
- Solt, I., Kulhanek, P., Simon, I., Winfield, S., Payne, M.C., Csányi, G., and Fuxreiter, M., Evaluating Boundary Dependent Errors in QM/MM Simulations, *J. Phys. Chem. B*, vol. **113**, no. 17, pp. 5728–5735, 2009.

- Stillinger, F. H. and Weber, T. A., Computer-simulation of local order in condensed phase of silicon, *Phys. Rev. B*, vol. **31**, no. 8, pp. 5262–5271, 1985.
- Svensson, M., Humbel, S., Froese, R. D. J., Matsubara, T., Sieber, S., and Morokuma, K., ONIOM: A multilayered integrated mo+mm method for geometry optimizations and single point energy predictions. A test for diels-alder reactions and Pt(P(t-Bu)(3))(2)+H-2 oxidative addition, *J. Phys. Chem.*, vol. **100**, no. 50, pp. 19357–19363, 1996.
- Tadmor, E. B., Ortiz, M., and Phillips, R., Quasicontinuum analysis of defects in solids, *Philos. Mag. A*, vol. **73**, no. 6, pp. 1529–1563, 1996.
- Thomas, L. H., The calculation of atomic fields, *Proc. Cambridge Philos. Soc.*, vol. **23**, no. 5, pp. 542–548, 1927.
- von Weizsacker, C. F., Zur theorie de Kernmassen, *Z. Phys.*, vol. **96**, pp. 431–458, 1935.
- Wang, L. W. and Teter, M. P., Kinetic-energy functional of the electron-density, *Phys. Rev. B*, vol. **45**, no. 23, pp. 13196–13220, 1992.
- Wang, Y. A., Govind, N., and Carter, E. A., Orbital-free kinetic-energy density functionals with a density-dependent kernel, *Phys. Rev. B*, vol. **60**, no. 24, pp. 16350–16358, 1999.
- Wang, Y. A., Govind, N., and Carter, E. A., Orbital-free kinetic-energy density functionals with a density-dependent kernel, *Phys. Rev. B*, vol. **64**, no. 8, p. 089903(E), 2001.
- Woo, T. K., Margl, P. M., Deng, L., Cavallo, L., and Ziegler, T., Towards more realistic computational modeling of homogenous catalysis by density functional theory: combined QM/MM and ab initio molecular dynamics, *ACS Symp. Ser.*, vol. **50**, no. 3-4, pp. 479–500, 1999.
- Zhang, X. and Lu, G., Quantum mechanics/molecular mechanics methodology for metals based on orbital-free density functional theory, *Phys. Rev. B*, vol. **76**, no. 24, p. 245111, 2007.
- Zhang, X. and Lu, G., Electronic origin of void formation in fcc metals, *Phys. Rev. B*, vol. **77**, no. 17, p. 174102, 2008.
- Zhang, X., Wang, C. Y., and Lu, G., Electronic structure analysis of self-consistent embedding theory for quantum/molecular mechanics simulations, *Phys. Rev. B*, vol. **78**, no. 23, p. 235119, 2008.
- Zhang, X. and Lu, G., Calculation of fast pipe diffusion along a dislocation stacking fault ribbon, *Phys. Rev. B*, vol. **82**, no. 1, p. 012101, 2010.